Transparent Antireflective Layers of Oxide Nanowires Grown from Thin Films by Pressurized Contact Interdiffusion Processes

Colm Glynn,[a] Laila Balobaid,[a] David McNulty,[a,*] and Colm O'Dwyer [a,b,*,z]

[a]*School of Chemistry, University College Cork, Cork T12 YN60, Ireland*
[b]*Micro-Nano Systems Centre, Tyndall National Institute, Lee Maltings, Cork T12 R5CP, Ireland*

Oxide phase nanowires are important for applications ranging from optoelectronics to water splitting, but prove difficult to grow in high density with good crystalline quality and phase purity. Heterogeneous catalysts are typically required to nucleate growth. This work demonstrates that dispersions of oxide nanowires can be formed directly from solution processed oxide thin films. We also examine the effect of changes in applied pressure between a solution processed vanadium oxide thin film and a surface-contacted glass coupon on the catalyst-free formation of interconnected sodium vanadate nanowire structures by interdiffusion. Under different applied pressures, meshes of high quality crystalline oxide nanowires formed on the surface, and we examine the nature of phase conversion and nanostructure growth including larger shards composed of multiple conjoined nanowires are also examined. The optical properties of the oxides NWs formed by interdiffusion from oxide thin films show promising properties for application as antireflective coatings across a broadband spectral range. This interdiffusion technique is effective for high quality oxide nanowire growth without catalysts directly from insulating or conducting thin films by direct contact with a source of diffusing species.
 [DOI: 10.1149/2.0371712jss]

Manuscript submitted October 11, 2017; revised manuscript received December 4, 2017. Published December 20, 2017.

The integration of nanowires (NWs) with modern devices and systems is advancing considerably each year with new applications, from electronics/optoelectronics to energy storage/generation, availing of these nanosized structures as active materials.[1–4] NWs can be made from a variety of materials each with their own specific applications, from metal to semiconducting NWs for use in applications such as transparent conducting electrodes, anti-reflection (AR) coatings, sensors, solar cells and photonics.[2,5–9] Improved methods for the incorporation of NWs with other device components, such as ensuring intimate electrical/thermal contact with the underlying substrate, requires better control and understanding of the NW growth processes. Investigation of improvements into the deposition methods for NWs also needs to focus on improved control over the growth, optical/electrical properties and site selectivity using a variety of techniques through both top-down and bottom-up processes.[10–13]

Applications such as transistor technologies require that there are no erroneous signals or crosstalk between each device; in situations such as this the growth and deposition technique of the NWs requires intricate and exacting methods to accomplish high site selectivity onto the substrates.[14,15] However, this site selective single NW deposition is not required for every application; instead large interconnected NW networks with random orientations are more desirable and also easier to deposit. Interconnected NW networks are used for catalysis, photonics and sensing applications where the random orientations, high surface areas and increased electrical connections improves the light absorption/scattering, sensor sensitivity and the electrical conductivity.[5,7,16–18]

The optical and optoelectronic applications of NW networks make them of particular use as conducting layers in transparent electronics, NW lasers, and as the active layer in solar driven energy devices.[5,19–21] When used as an active layer in a device, such as a conducting layer or working electrode, the NW material must be chosen based on the specific attributes required for the application. In most cases these required attributes dictate whether a NW for an application must be a semiconductor, metal or oxide material. When used as secondary components of a device, such as an AR coating or hydrophobic layer for photovoltaics, the NWs do not require specific thermal or electrical attributes and the number of applicable materials increases. For example, NW based AR coatings have been developed using a variety of materials ranging from silicon, silver and also metal oxides such as ZnO/MgO to achieve low reflectivity.[2,22–24] NW-based AR coatings can decrease the reflectivity of a device without the requirement of a multi-layered morphology such as used for thin film AR coatings.[25]

The growth parameters required for the formation of various NW networks can be a limiting factor in the type of material which is suitable for a device. NW networks are deposited using numerous top-down and bottom-up methods including vapor, physical and chemical techniques.[13,19,26–28] These deposition techniques require the use of either pre-deposited nanoparticle catalysts for large areal coverage or post-growth dispersion by depositing pre-formed NWs onto choice substrates. A stable and intimate contact to the substrate can be achieved using many of the above top-down and bottom-up deposition techniques, however, if not removed the remnant catalysts can be detrimental to device performance, such as Au contamination in silicon NWs.[29] New methods for the growth and deposition of pure NWs onto industrial relevant substrates must be investigated for the formation of high quality and pure materials.

Solution processing approaches can be used to deposit high quality and pure NW networks onto substrates. Solution processing techniques incorporates a range of facile deposition techniques including spin- and dip-coating where the process can be reliably scaled.[30,31] For most solution processed approaches, the spin- and dip-coating techniques are used for depositing either pre-grown NWs or the nanoparticle catalysts onto the substrate surface.[32,33] High quality metal oxides with unique crystal structures and compositions are under investigation for various applications but are difficult to grow at low temperatures without the use of complex liquid or vapor precursors.[27] Instead of solely using solution processed methods for the deposition of pre-formed NWs, we suggest a method which utilizes the large surface coverage capabilities of solution based techniques and combining them with an interdiffusion process for the direct formation of high quality NWs without the requirement of catalyst materials.

Previously, we have demonstrated a method for the growth of NW networks through interdiffusion between a solution processed vanadium oxide thin film with a contacted donor glass.[34] The technique does not require the use of pre-placed catalysts and instead utilizes a temperature driven phase conversion using to-down solid state contact interdiffusion where the diffusion of species from a donor and acceptor material occurs.[30,34,35] The role of applied pressure between the contacted donor glass and the solution processed thin film on the growth of NW networks was examined and related to the optical characteristics of the $NaVO_3$ based NWs. The AR properties of the $NaVO_3$

*Electrochemical Society Member.
[z]E-mail: c.odwyer@ucc.ie

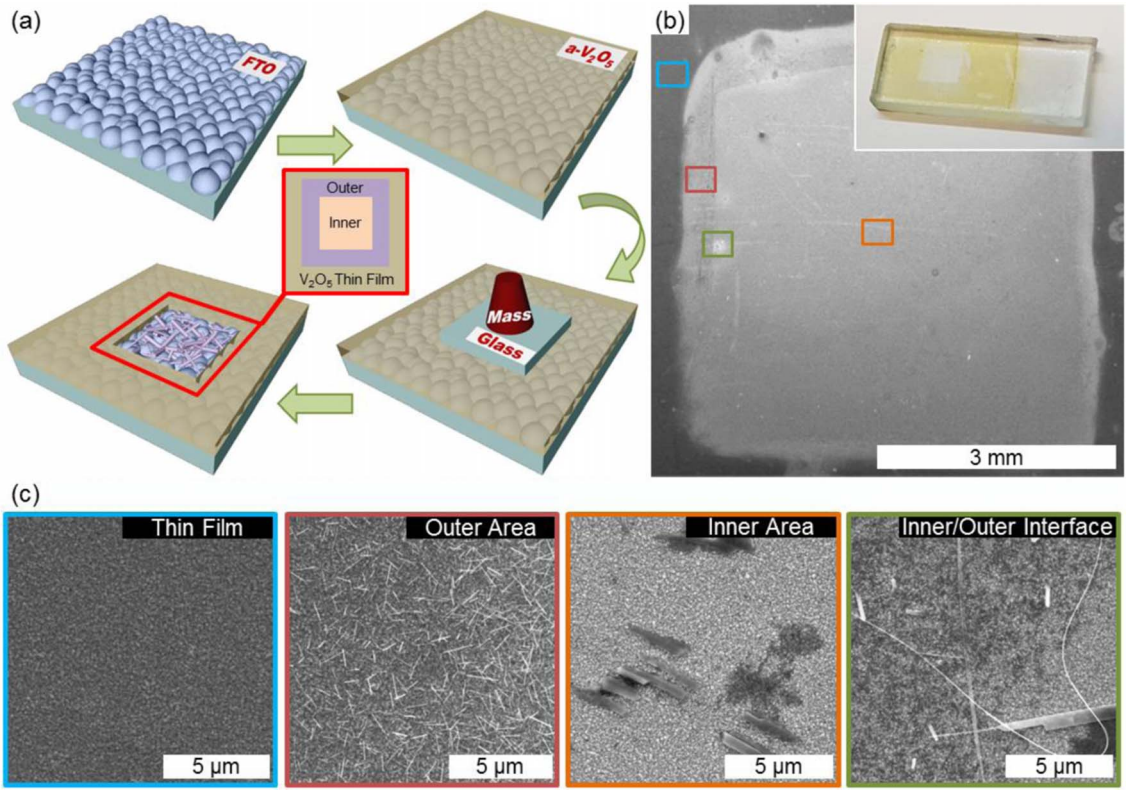

Figure 1. (a) Schematic of the experimental procedure showing the contact interdiffusion process. (b) SEM image of an interdiffused region formed at a pressure of 593 Pa. The inset shows an optical image of the sample after thermal annealing and removal of the contacted glass. (c) SEM images of oxide nanostructures formed in the regions (color coded) drawn in (b).

NWs and its effect on the reflectance properties of the FTO on glass substrate is examined. $NaVO_3$ is a colorless material with high levels of transmission as previously shown when formed as a cohesive thin film.[36]

Here, the effect of pressure between the a-V_2O_5 thin film and contacted glass on the nucleation and growth of NW networks is examined. In particular, we show that the nature of oxide NW formation is sensitive to the pressure applied to a thin film evenly coated over a textured surface, providing nucleation points for subsequent crystal growth of a new crystalline phase caused by interdiffusion of Na- species from the top-contacted glass substrate. We present a detailed examination of the composition, structure and morphology of the NWs as a function of applied pressure, demonstrating region-specific NW growth habit from the oxide thin film. Finally, these oxide NW network layers are shown to be promising AR coatings across a broadband spectral range.

Experimental

Prior to contact interdiffusion, thin films of amorphous V_2O_5 (a-V_2O_5) were deposited onto 350 nm thick fluorine-doped tin oxide (FTO) coated glass substrates from a 1000:10:1 (IPA: Alkoxide: H_2O) precursor solution. The initial a-V_2O_5 thin films were dip-coated using a PTL-MM01 desktop dip coater at a constant withdraw rate of 2.5 mm/s. For depositing an a-V_2O_5 thin film with a thickness of ∼30–45 nm, three iterative dip-coats, each coated after allowing sufficient time for the previous layer to hydrolyze and dry, are deposited onto the FTO substrate. Prior to the surface contacting and thermal annealing steps, UV-O_3 cleaning of the a-V_2O_5 and glass surfaces using a Novascan UV-O_3 system was conducted for 1 h. Clean borosilicate glass (composition: SiO_2: 72.20%, Na_2O: 14.30%, CaO: 6.40%, MgO: 4.30%, Al_2O_3: 1.20%, K_2O: 1.20%, SO_3: 0.30% and Fe_2O_3: 0.03%) was placed in direct contact with the a-V_2O_5 surface.

Different masses were placed on the glass substrate to study the role of pressure on localized NW formations. An enclosed furnace was used for annealing the samples at 450°C with an ambient atmosphere. The samples were heated at a rate of 5°C/min and held at 450°C for 6 h. Contact interdiffusion was also performed directly on non-oxidized Si substrates as a comparison using the same deposition procedures.

Surface morphology of the samples was examined by scanning electron microscopy (SEM) performed on an FEI Quanta 650 FEG high resolution SEM with operating voltages of 10–20 kV equipped with an Oxford Instruments X-MAX 20 large area Si diffused EDX detector. Image analysis of the NWs on the surface was performed using an edge detection and greyscale intensity thresholding technique from the ImageJ software package.[37,38] AFM analysis was performed on a Park XE-100 AFM system in non-contact mode with SSS-NCHR enhanced resolution tips, the XY and Z resolution are ∼ 2 nm and 0.05 nm, respectively. Raman scattering spectroscopy was collected on a Renishaw InVia Raman spectrometer using a 514 nm, 30 mW laser source. Spectra were collected and focused onto the samples using a 50 × objective lens. Angle-resolved transmission and reflectance UV-Vis-NIR spectroscopy was performed using a custom built apparatus with spectra recorded on OceanOptics USB2000+ and NIRQuest 512 spectrometers for UV-Vis and NIR spectral regions, respectively. The light was focused to a 1 mm spot size from a broadband halogen light source. Transmission measurements at normal incidence angle are presented with both air and separately the substrate (glass + FTO) as the background.

Results and Discussion

Oxide NW morphology and surface density.—The technique for depositing NW networks by contact interdiffusion is outlined in Figure 1a. The FTO-coated glass substrate was sequentially dip-coated with three layers of a-V_2O_5. Each dip-coated layer has an approximate thickness of ∼10 – 15 nm with an overall a-V_2O_5 layer thickness of

Table I. Information on the substrates and applied pressure for the samples studied.

Substrate	Applied Mass (g)	Applied Pressure (Pa)	Temperature (°C)
FTO	0.06	23	450
FTO	9.90	396	450
FTO	29.58	593	450
Si	9.90	396	450

~30 – 45 nm. A clean borosilicate glass coupon is contacted to the a-V_2O_5 thin film surface and the applied pressure is varied between 23–593 Pa using the glass coupon and individual aluminum (Al) masses of 9.84 g, each placed on the a-V_2O_5 over an area of 2.5×10^{-5} m^2. Table I summarizes the different applied masses and pressures for each sample we investigated.

Figure 1b shows an SEM and optical image of a square-shaped region created by the interdiffusion between the Na species in the contacted glass coupon, and the V_2O_5 thin film at a pressure of 593 Pa. Higher resolution images of the different regions highlighted with the colored frames is shown in Figure 1c; the V_2O_5 thin film, inner, outer and interface regions. The region surrounding the interdiffused square is composed of crystalline orthorhombic V_2O_5. Within the contacted interdiffused square area, we observed two distinct regions, inner and outer, with different surface morphologies which are separated by a distinct interface. Corresponding SEM images of the interdiffused squares formed at applied pressures of 23 Pa and 396 Pa is shown in Supporting Information Figure S1.

Various types of surface morphology were produced within the contacted square region as the pressure is increased. Previously, we showed that interdiffusion occurs between Na-containing borosilicate glasses and a-V_2O_5 thin films. In that particular case, a conformal a-V_2O_5 thin film coated onto Na-containing glass substrates without any diffusion barrier coating ensured interdiffusion caused conversion to a coherent $NaVO_3$ film that followed the morphology of the substrate, whether it is rough or smooth.[35,36,39] Interdiffusion that occurs between top-contacted glass and an a-V_2O_5 thin film (on a surface other than the glass),[34] NW growth occurs from the thin film that follows the growth habit of the crystalline oxide phase caused by interdiffusion of Na species. The influence of the nature of the interface between the glass and initial oxide thin film on the growth of NWs with regard to the influences of pressure, thermal contact and the optical properties of the NW networks were not previously examined.

The SEM images of Figure 2 shows how the NW features form within the inner regions of the interdiffused area that underwent annealing with applied pressures of (a) 23 Pa, (b) 396 Pa and (c) 593 Pa. At the lowest applied pressure of 23 Pa (contacted glass coupon alone), the inner region contains NWs with a uniform width interspersed on the surface. The higher resolution SEM images of Figure 2a show the remnants of the a-V_2O_5 thin film on the surface, which was not transformed to NWs. By increasing the applied pressure to 396 Pa and 593 Pa respectively, larger shards of material are formed by the interdiffusion process, from a similar initial oxide thin film. At higher applied pressure, we did not detect any remnants of the a-V_2O_5 thin films on the surface of the inner region (further detail in Supporting Information Figure S2).

SEM images of the surface of the outer region formed at applied pressures of 23, 396 and 593 Pa is shown in Figures 3a–3c respectively. At the lower applied pressure of 23 Pa, the surface in the outer region shows the onset of NW formation on the surface by recrystallization from interdiffusion with the contacted glass species. From the SEM evidence in Figure 3a, a larger amount of the non-interdiffused a-V_2O_5 thin film remnant remains on the surface compared to the respective inner region shown in Figure 2a. The remnant of the a-V_2O_5 thin film has not undergone interdiffusion and formed a crystalline vanadium oxide rather than contributing to the formation of the NWs.

SEM images of the outer regions for the higher applied pressures of 396 Pa and 593 Pa are shown in Figures 3b, 3c respectively. These outer regions show the formation of dense NW networks on the surface of the FTO rather than the larger shards/NW bundles. With the increase in the applied pressure to 396 Pa, the remnants of the a-V_2O_5 thin film are less apparent on the FTO surface as seen in Figure 3b compared to the remnants on the surface formed at 23 Pa. This is evident by the increased number and size of the NWs grown which would require the vanadyl species from the a-V_2O_5 thin film. At the

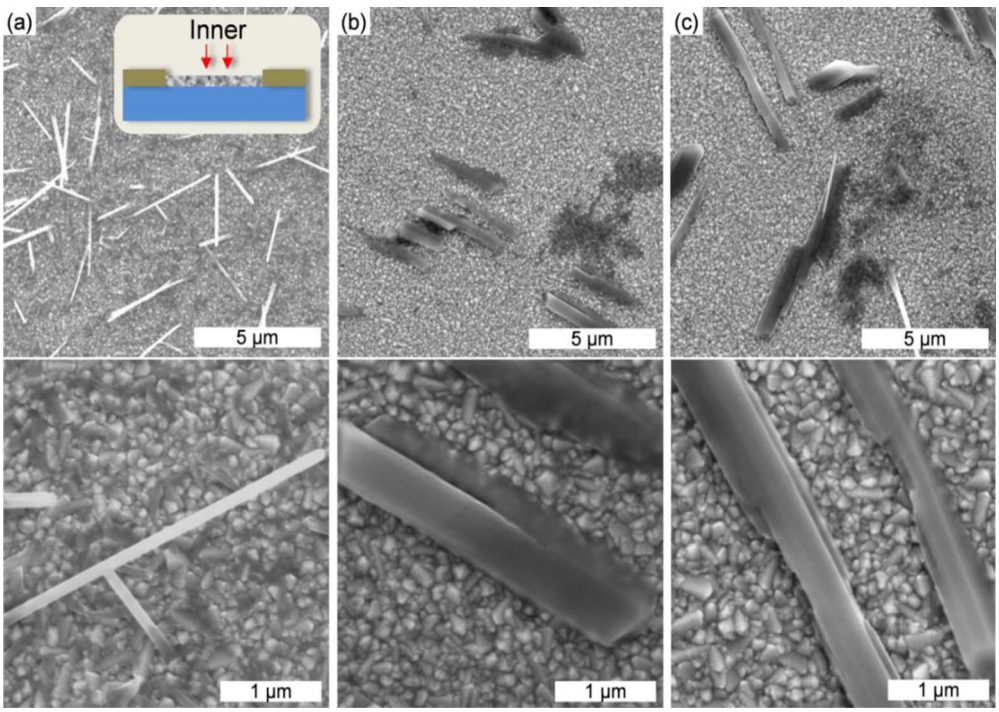

Figure 2. SEM images of the NW structures within the inner region formed at applied pressures of (a) 23 Pa, (b) 396 Pa and (c) 593 Pa through interdiffusion processes.

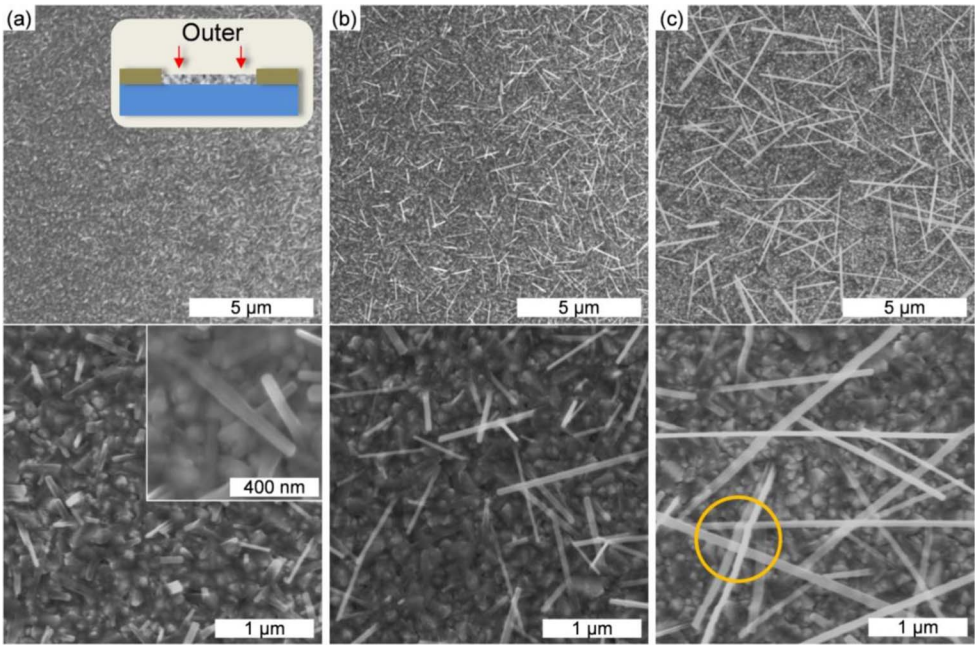

Figure 3. SEM images of the outer region showing the NW structures and a-V_2O_5 thin film remnants formed at applied pressures of (a) 23 Pa, (b) 396 Pa and (c) 593 Pa through interdiffusion processes. The lower set of images are higher magnification regions of the top row. The circled region shows the intimate contacts between the NWs that grow out from the surface.

highest applied pressure of 593 Pa, SEM images in Figure 3c show that there is no discernible a-V_2O_5 thin film remnant remaining on the surface. This process is clearly quite sensitive to relatively small changes in applied pressure, where nominal values are a fraction of sea-level atmospheric pressure. For the samples prepared at applied pressures of 396 Pa and 593 Pa, a distinct interface region is found between the inner and outer regions as shown in Figures 4a, 4b, respectively. At an applied pressure of 396 Pa, NW meshes are observed at this interfacial region. Interdiffusion that occurs at a higher applied pressure of 593 Pa facilitates the formation of thick NW meshes be-

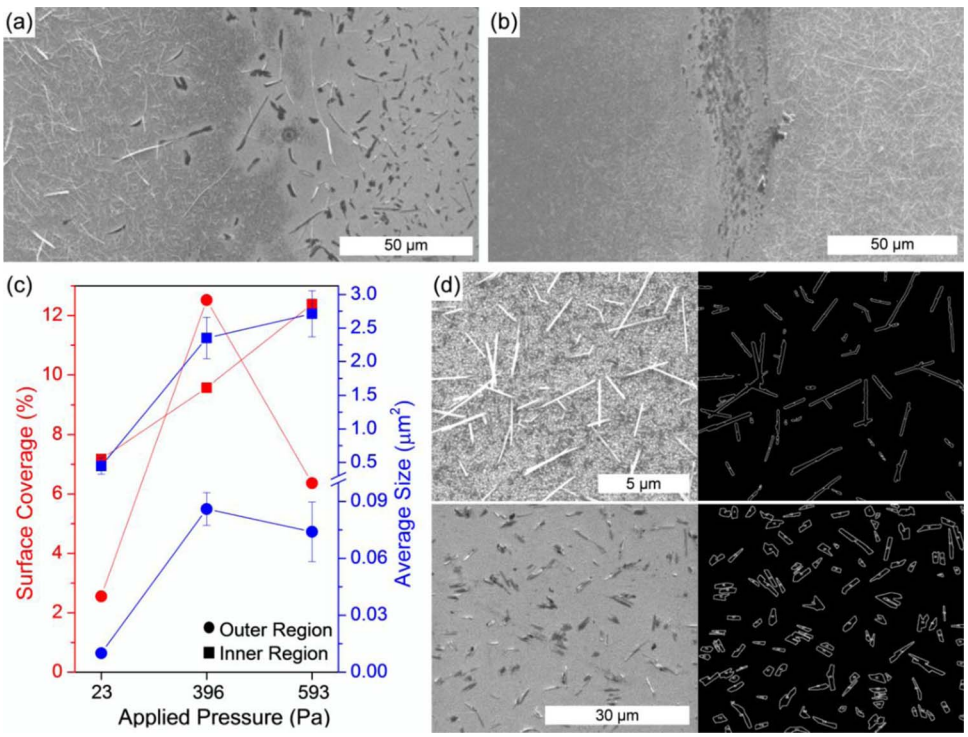

Figure 4. SEM images of the interface region between the inner and outer areas at applied pressures of (a) 396 Pa and (d) 593 Pa. (c) Comparison of average surface coverage and size of the NWs/shards for the inner/outer surface areas at different applied pressures. Error bars were calculated from standard deviation of the average size and surface coverage between sampling areas. (d) Examples of NW/shard surface area and size analysis images formed through removal of the substrate background and edge detection/thresholding of the nanostructures.

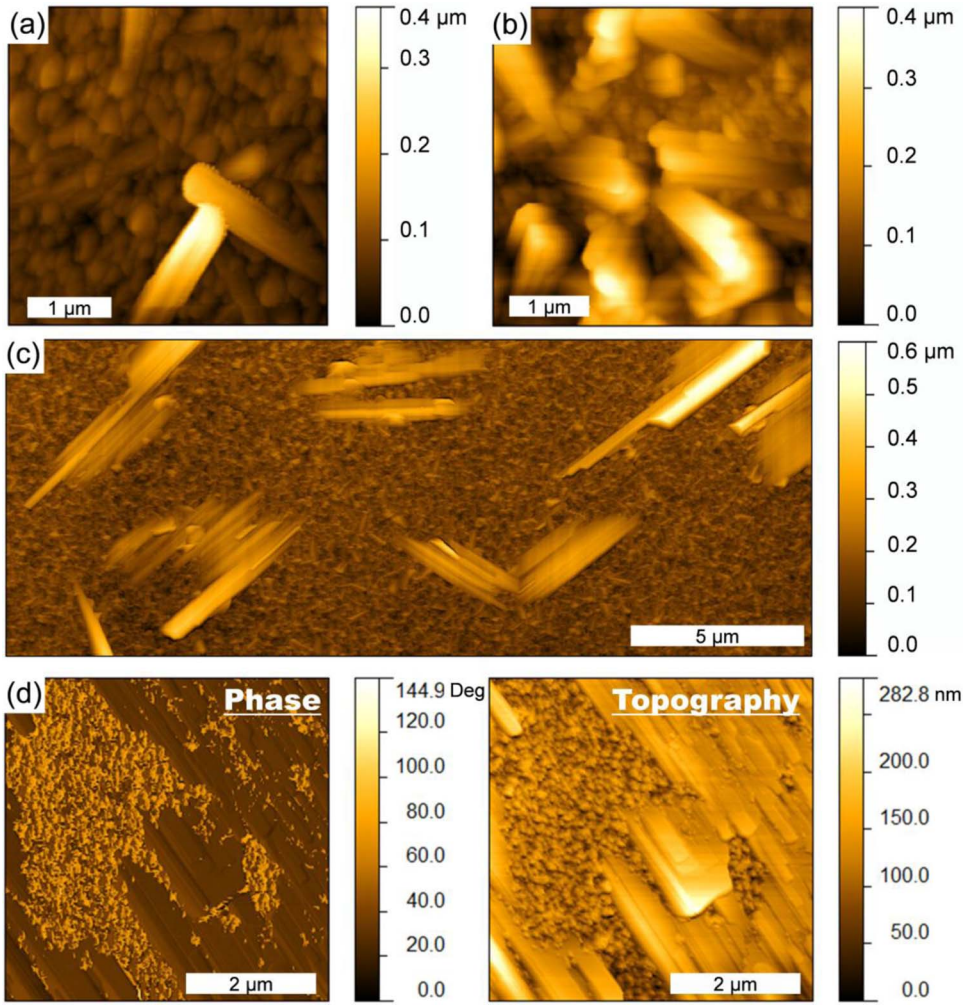

Figure 5. AFM images of the (a) inner and (b) outer areas formed at an applied pressure of 23 Pa. (c) AFM images of the shards formed within the inner area of a sample formed at 593 Pa showing the clumped morphology. (d) Phase and topography AFM images of both FTO and shard/NW materials.

tween the inner/outer interface; the density of shards decreases and instead the surface is coated by NW recrystallized from the original thin film. NWs eventually grow away from the surface, yet intimate contacts observed between NWs (see circled region in Figure 3c) suggest that NW nucleation and density is defined in the early stages. An example of the NW mesh formed close to the inner side of the interfacial region at 593 Pa is shown in Supporting Information Figure S3.

The average size and surface coverage of the NWs formed by contact interdiffusion as a function of pressure and location on the surface, was carried out by SEM image analysis, and shown in Figure 4c. During the image analysis, the FTO background is removed and the size and surface coverage of the NWs/shards is calculated, examples of the image analysis used to calculate the average size and surface coverage of NWs and shards are shown in Figure 4d (see Supporting Information Figure S4 for further examples). The larger average sizes ($\sim$0.5 – 2.5 μm^2) calculated for nanostructures formed at the inner regions at pressures of 396 Pa and 593 Pa is due to the formation of the shards as opposed to the smaller NWs observed at lower pressures, and as a NW network or mesh, the surface coverage is greater ($\sim$12%) while the average sizes are the smallest measured for this system. Analysis of different areas of each region shows that in the outer interdiffused regions NWs of various sizes are typically formed and this is consistent for each applied pressure. Our analysis suggests that a significant increase in the NW size is caused by a higher pressure between the a-V_2O_5 film and glass coupon.

AFM imaging was employed to study the interaction and structuring between the FTO substrate and interdiffused NWs. AFM images of the NWs formed on the surface within the inner and outer areas for a sample formed at an applied pressure of 23 Pa is shown in Figures 5a, 5b, respectively, with the granular FTO substrate clearly visible underneath the NWs. The variation between the inner and outer regions of the NWs is apparent in the AFM images, where the inner region has singular NWs with bundled NWs characteristic to the outer region. It is clear from the AFM images that the ends of the NWs protrude from the surface of the FTO substrate. Oxide NW growth proceeds away from the rougher surface, even when sandwiched between the overlaid glass and the film that coats the underlying FTO.

AFM image evidence of the NW shard structures grown post interdiffusion at an applied pressure of 593 Pa shown in Figure 5c confirm that the shards which form are composed of conjoined NWs which have grown in a single direction, presumably initiated from a similar region of the surface film at the same time. These bundles of NWs merge into singular large structures from the V_2O_5 film on the surface of the FTO instead of following separate randomly oriented growth from dissimilar nucleation times. The NW mesh coverage is distinctly different, and NWs nucleate from interdiffusion and phase conversion within the film, at different times while avoiding bundle formation. The comparison between phase and topography AFM images for a region containing FTO substrate and shards is shown in Figure 5d. We analyzed the initial stage of growth using phase imaging to distinguish between FTO, remnant V_2O_5 film and the nucleation and

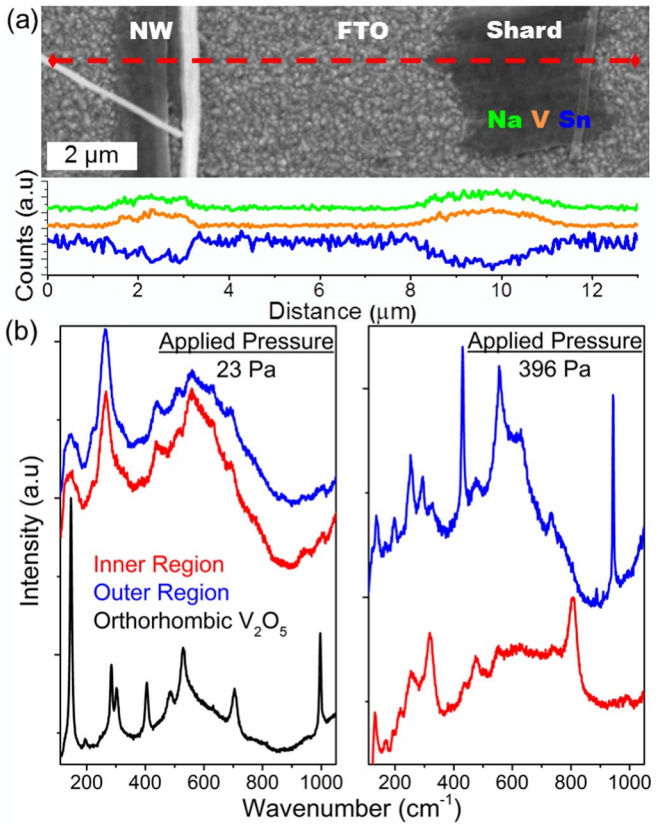

Figure 6. (a) Elemental EDX line map across a shard and NW showing the distribution of Na K, V K X-ray emission from the nanostructures and Sn L emission from the underlying FTO substrate. (b) Raman scattering spectra of oxide NWs at the inner and outer regions at 23 and 396 Pa pressure.

initial growth of NWs and shards. The AFM phase image in Figure 5d shows that the bundled NW shards are composed of the same material and their morphology is similar to V_2O_5 nanofibers,[40] and thus it is likely that structural modification into fibers occurs from the film that subsequently converts to the $NaVO_3$ phase. We previously proved that the initial stages of the nanostructure film are $NaVO_3$ (vide infra).

Structure, composition and antireflective properties.—The composition of the interdiffused NWs was examined using a combination of EDX and Raman scattering spectroscopy, presented in Figures 6a, 6b. An EDX line scan was acquired across an interfacial region in Figure 6a between the inner and outer regions of the contact region after typical heating while at a pressure of 396 Pa, to enable both NWs and shards to be examined. X-ray emission from V K, Na and Sn L shells were probed and overlaid on the SEM image. The intensity of V K and Na K lines increase similarly in the vicinity of the regions where both NWs and shards are present. The EDX analysis demonstrated that while the rough surface of the FTO surface affects the formation of the NWs during contact interdiffusion, there is no Sn, within the detection limit, found within the NWs.

Raman scattering spectroscopy in Figure 6b was used to examine the crystalline structure of the NWs on the FTO surface formed at each applied pressure. The surrounding a-V_2O_5 areas which have not been contacted with the donor glass crystallize to orthorhombic V_2O_5 after thermal annealing. We did not find evidence of cation diffusion or interaction with the underlying SnO_2 in the FTO. As was shown previously, the formation of $NaVO_3$ occurs due to interdiffusion between Na species within borosilicate glass and the a-V_2O_5 thin films. The glass substrate is effective at providing Na species for interdiffusion when conformally coated with a-V_2O_5, and in cases where interdiffusion is not desired, layers such as FTO or thick SiO_2 can act as diffusion barriers.[34,35,41] Raman scattering spectroscopy of Figure 6b shows that evidence of phonon modes from two crystalline phases of $NaVO_3$, α- and β-phases, which are formed and detected in the inner and outer areas. The Raman scattering spectra for the inner and outer areas on samples formed at applied pressures of 23 Pa shows some small modes corresponding to orthorhombic V_2O_5 from crystallized regions of the initial a-V_2O_5 thin film which was not converted to NWs.

Growing oxide phase NW layers has received limited attention compared to semiconducting NW growth, often because the control over morphology for transition metal oxide in NW is difficult without heterogeneous seeded growth methods.[27] Nanowires in the form of surface layers also act as graded index materials, and optical transmission or antireflective properties in the visible spectrum can be enhanced using visibly transparent oxides in dispersed NW form.[13,42] The angle-resolved UV-Vis optical characteristics of the NWs were examined in both reflection and transmission spectroscopy modes. Figure 7a shows the transmission spectra at 0° (incident) angle for the complete system: FTO, V_2O_5 and the contact interdiffused NW regions formed at 23 Pa, 396 Pa and 593 Pa, respectively. The transmission through the entire sample shows that the oxide NW mesh predominantly causes optical scattering at wavelengths >500 nm, reducing the overall transmission. The optical transmission through the NW layer formed at 23 Pa exhibits an absorption edge at ∼510 nm that is similar to the V_2O_5 thin film. This absorption arises from remnant a-V_2O_5 on the FTO surface which is evident on the surface in the SEM images of Figure 3a. The SEM images of Figure 3b also show thinner and sparser remnants of thin film areas on the surface of the outer regions formed at 396 Pa. A corresponding absorption edge of a-V_2O_5 on the surface is not seen in the UV-Vis spectra after conversion at 396 Pa pressure. This suggests that the remnants visible on the surface at applied pressures of 396 Pa may be an intermediate stage prior to the formation of the $NaVO_3$ NWs and thus do not exhibit the same optical absorption of the a-V_2O_5 band edge. Thus at higher applied pressures, such as 593 Pa, these remnants form the $NaVO_3$ NWs outright where no remaining film is seen. Optical transmission for the regions with little to no V_2O_5 remnants and predominantly coated with oxide NWs, exhibits a plateau below 500 nm, where conversion to an effective low-k porous film of $NaVO_3$ NWs eliminates optical absorption from the V_2O_5 film. The conversion to oxide NWs reduced Fresnel reflection and eliminates interference characteristic of a reflective thin film.[43–45]

NW coatings on substrates are a common method for AR and anti-glare applications.[2,24] Engineering surface texture by nanostructured coatings[46] has been demonstrated by E-beam lithography,[47] polymer replication,[24,48] feature etching,[49] and by oblique angle deposition[25] to create graded index layers, which also have the advantage of improve light extraction efficiency in light emitting devices,[50] or improving light collection in solar cells.[51,52] Angle-resolved UV-vis spectra in both transmission and reflection configurations was carried out on NW dispersions directly grown from oxide thin films on FTO-coated glass substrate to assess their AR properties. Figure 7b demonstrates that oxide NW coverage consistently maintain an equal or greater optical transmission across the visible spectrum than the original V_2O_5 film. The corresponding UV-vis spectra for each sample and region are shown in Supporting Information Figures S5 – S6. Converting the V_2O_5 film on FTO into oxide NW dispersions particularly improves transmission at or below the absorption edge of the original film by a factor of 3, and is marginally more transparent in the spectral range where absorption of the original film is at a minimum. The NW layers formed from V_2O_5 on an FTO substrate also improve AR characteristics (allow greater transmission) through the entire sample from 30–60° from normal incidence compared to either FTO-coated glass or a V_2O_5 film on FTO. Porosity within the NW layer improves transmission compared to V_2O_5 and removed direct bandgap absorption losses from the film. Impedance matching with the air interface from the porosity of the NW mesh, and elimination of the absorption of the V_2O_5 film suppresses Fresnel reflections across the

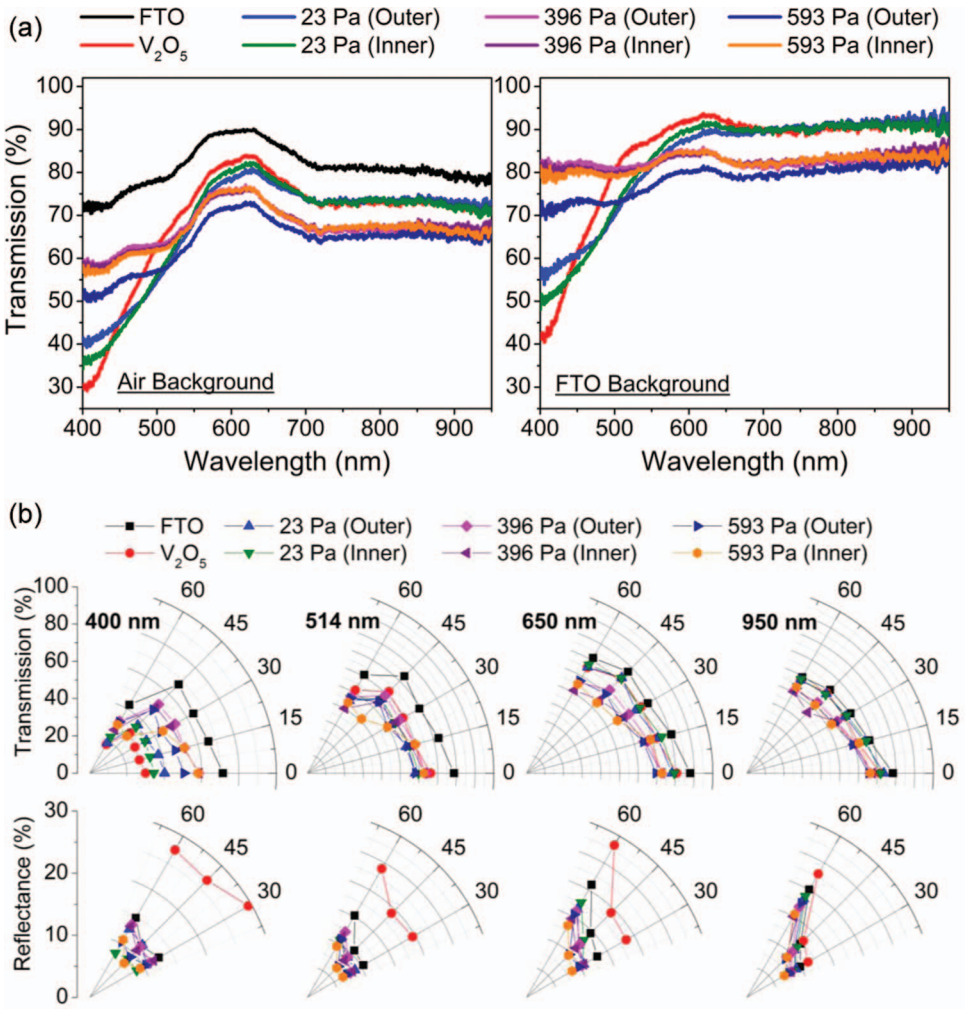

Figure 7. (a) UV-vis Transmission spectra at 0° incident angle of various regions of samples formed at 23 Pa, 396 Pa and 593 Pa compared to an air (no substrate) background and factoring background transmission through the FTO/Glass substrate. (b) Transmission and reflectance measured at 400 nm, 514 nm, 650 nm and 950 nm at various incident angles from 0–60° (transmission) and 30–60° (reflectance). A gold film standard was used as reflectance reference at each angle, see Supporting Information Figure S7.

visible spectrum. The characteristic angle-dependent reflectance of the film is essentially removed by conversion to the porous NW mesh morphology as the $NaVO_3$ phase.

Role of interfacial contact on interdiffusion.—The role of the FTO surface roughness and applied pressure of the a-V_2O_5 coated FTO interfacial contact to the smoother glass coupon was examined in the context of thermal contact resistance (TCR). NW formation from the a-V_2O_5 film by phase conversion is facilitated by interdiffusion during thermal annealing. Surface analysis demonstrates how contact pressure influences the density and size of the oxide NWs and nanostructures. The theory of TCR relates the transport of thermal energy across interfacially contacted materials and the role of surface roughness discrepancies between the two materials.[53–55] Between two contacted materials, the interface contact is not perfect due to surface roughness; instead the interface contains localized regions of physical contact, i.e. at the apices of peaks in the roughness profile of the rougher surface. Figure 8a diagrammatically shows this scenario for the oxide film-to-NW conversion studied in this work. The thickness of the FTO is 350 nm with the topmost granular surface having a measured R_{rms} roughness value of 8.2 nm. The smoother glass coupon physically contacts an a-V_2O_5 coated FTO/glass substrate at a low applied pressure (mass of the glass) at a finite number of contact points, where the average rms roughness (R_{rms}) of the two surfaces is 0.3 and 8.2 nm respectively. The order of magnitude difference in the roughness between the FTO substrate and the contacted glass ensures that the glass touches only at the apices of the FTO roughness features that are coated by the oxide film.

Thermal energy transfer during the initial heating ramp from ambient to equilibration to the a-V_2O_5 surface is important for both interdiffusion processes and crystallization. The direction of heat flow can be approximated by examining the thermal resistances of the materials above and below the a-V_2O_5 and glass coupon contact. The thermal resistance of substrate, when in contact, can be estimated using a simplified version of Fourier's Law of conduction, $R_T = \frac{L}{kA}$, where R_T is the total thermal resistance of the material, L is the length of heat flow, k is the thermal conductivity of the material and A is the area perpendicular to heat flow.[56] The effect of the thermal resistance of the thin film coating on the FTO/glass substrate was negligible as it is several orders of magnitude thinner than the glass. At nanoscale values, the thermal resistance calculations from Fourier conduction differs significantly as the length scales of materials approach the characteristic lengths of heat carriers, thus the role of the macroscale substrates with heat flow to the a-V_2O_5/glass interface was examined.[57,58] The R_T value for heat flow through the glass coupon (1 mm thickness, k = 1 W/mK) to the a-V_2O_5 thin film was calculated to be ~ 40 K/W while heat flow through the bottom of the FTO coated glass substrate (3 mm thickness) is ~ 120 K/W (the contacted surface area between the a-V_2O_5 and glass is 2.5×10^{-5} m^2). The lower thermal resistance of the glass substrate to the a-V_2O_5 implies faster initial heat flow in

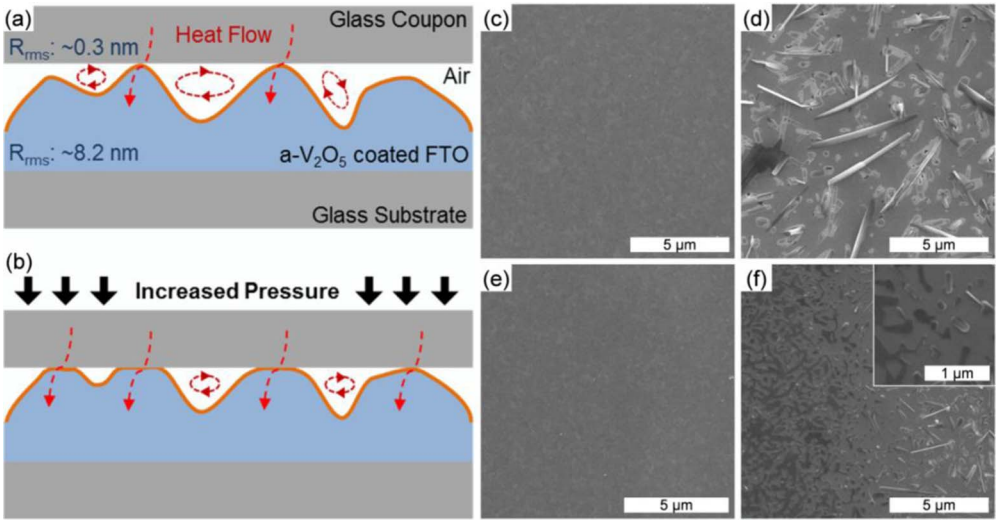

Figure 8. (a, b) Schematic showing the effect of increased pressure on the contact between the glass coupon and the a-V_2O_5 coated FTO substrate at two different applied pressures respectively. The R_{rms} values of the two contacted surfaces are given. SEM images of contact diffused region on Si substrate showing the (c) thin film, (d) inner, (e) outer and (f) interface regions.

this direction compared to heat flow from the bottom up as the entire system is initially heated, even in cases where the applied pressure is increased using additional Al masses (each mass is 6 mm thick, k = 205 W/mK). The R_T value for the top surface increases at the highest applied pressure of 593 Pa to 43.5 K/M.

In a low applied pressure scenario, the glass coupon and a-V_2O_5 are contacted only at the apices where the surfaces connect. The heat flow with the "valley" areas between FTO roughness features is of course less than at physical contact points as heating requires convection in the air gap as highlighted in Figure 8a. In a contacted case, the a-V_2O_5 conformally coats the glass surface, which results in film-glass thermal contact points at the apices of roughness features on the underlying granular FTO substrate. It is from these thermal contacts that the interdiffusion initiates into the thin film. The Na species cannot "jump" across an air gap and so must be transferred across the thermal contacts. In such a case, this mechanism suggests that the a-V_2O_5 regions in the valleys of the surface are not interdiffused with Na at the same time as regions in contact with the glass. Instead of forming $NaVO_3$ through interdiffusion these regions crystallize into vanadium oxides as sufficient time has passed for convection processes to anneal the material. This process leaves remnant crystalline V_2O_5 on the FTO surface.

When increased pressure is applied on the glass coupon, we propose qualitatively that the physical contact surface area increases because lower height apices of the film-coated FTO surfaces come into contact with the glass, shown diagrammatically in Figure 8b.[53,54,59] In this case, the heat flow across contacts will increase and allow for more Na species for interdiffusion and also decrease the number of regions where convection will cause the formation of vanadium oxides. There is an order of magnitude difference in the R_{rms} between the glass and a-V_2O_5 coated FTO surfaces, however, the values are on the order of nm indicating that the amount of extra strain that would be required to contact other surface apices through deformation of the FTO would be small. Therefore, at increased applied pressures, as is the case of samples prepared at 396 Pa and 593 Pa, more interdiffusion occurs in the initial stages of heating, preferentially form the glass to the contacts to the film, and less of the remnant V_2O_5 is present, after thermal annealing.

Finally, to test the role of the interfacial contact and thermal resistance at contact points to a rough surface, a similar test was performed at an applied pressure of 396 Pa using an a-V_2O_5-coated Si substrate. In this case, the Si substrate replaces FTO coated glass and has a surface roughness that is equivalent to that of the glass substrate (<0.2 nm). Figures 8c – 8f shows the SEM images of the resulting thin film, inner, outer and interface regions on the Si substrate. The thin film region is also uniformly coated by V_2O_5, just like FTO substrates. The inner region shows the formation of large needle like structures on the surface, with evidence of "lift-off" which may have occurred during removal of the contacted glass. No evidence of NW formation was found in the main outer regions with only some apparent thin film dewetting effects seen at the interface (Figure 8f) between the two regions, suggesting that the outer region is composed of a film instead of spatially localized NWs. Supporting Information Figure S8 shows higher magnifications of the specific regions with a large overview of the contacted square.

The results shown in Figures 8c–8f suggest that when an increased number of thermal contacts exists between the glass coupon and the a-V_2O_5 substrate then the formation of larger structures through interdiffusion dominates as found in the inner regions of the samples formed on FTO at applied pressures of 396 Pa and 593 Pa. The increased pressure will also limit the space for NW growth, with the area free space between the interdiffusion source and the growth areas decreased the NWs may be forced together to make larger shards as demonstrated with the AFM image of Figure 8f.

Conclusions

The effect of pressure on interdiffusion processes during the formation of interconnected $NaVO_3$ NW structures between an a-V_2O_5 coated FTO substrate contacted to a Na-species containing glass coupon was investigated. The effect of changes in applied pressure at the interface between the glass coupon and the a-V_2O_5 thin film was assessed with regards to the resultant NW surface coverage, size and optical properties. Interdiffusion between the glass coupon and thin film formed both $NaVO_3$ NW meshes and larger shards. The shards are composed of conjoined NWs which nucleated grew together during the thermal annealing stage. At lower applied pressures, remnant crystalline V_2O_5 remains on the surface with the interdiffused since interdiffusion of Na species is slower than the crystallization of the a-V_2O_5 due to a reduced number of physical contact points between the a-V_2O_5 on the rough FTO surface, and the glass coupon. The remnant crystalline V_2O_5 is not present when a higher applied pressure, >593 Pa, is utilized because a larger surface area is contacted between the a-V_2O_5 and the glass coupon; all material is recrystallized to oxide nanowire structures. The oxide NW meshes and conversion from V_2O_5 are promising for application as AR coatings across a broadband spectral range, especially as the method involves the conversion of a pre-deposited thin film. Compared to the underlying FTO-coated glass

and the crystalline V_2O_5 film on FTO the $NaVO_3$ NW meshes have improved AR characteristics in the 30–60° range. Interdiffusion using top contacts is an effective means of localized phase and morphology conversion of oxide thin films into oxide NWs without the use of heterogeneous catalyst, leaving a mesh of oxide NWs intimately contacted to the substrate surface. The approach in general may be useful for inspiring complex oxide nanomaterials based on the composition of a pre-deposited oxide thin film from optics and nanoelectronics, to water splitting or electrocatalysts.

Acknowledgments

This work was also supported by Science Foundation Ireland (SFI) under a Technology Innovation and Development Award 2015 under contract 15/TIDA/2893.

ORCID

Colm O'Dwyer https://orcid.org/0000-0001-7429-015X

References

1. Y. Li, F. Qian, J. Xiang, and C. M. Lieber, *Mater. Today*, **9**(10), 18 (2006).
2. P. Hiralal, C. Chien, N. N. Lal, W. Abeygunasekara, A. Kumar, H. Butt, H. Zhou, H. E. Unalan, J. J. Baumberg, and G. A. J. Amaratunga, *Nanoscale*, **6**(23), 14555 (2014).
3. M. Le Thai, G. T. Chandran, R. K. Dutta, X. Li, and R. M. Penner, *ACS Energy Lett.*, 57 (2016).
4. J. Tang, Z. Huo, S. Brittman, H. Gao, and P. Yang, *Nat. Nano*, **6**(9), 568 (2011).
5. J. H. Chang, K. M. Chiang, H. W. Kang, W. J. Chi, J. H. Chang, C. I. Wu, and H. W. Lin, *Nanoscale*, **7**(10), 4572 (2015).
6. T. J. Kempa, R. W. Day, S. K. Kim, H. G. Park, and C. M. Lieber, *Energ. Environ. Sci.*, **6**(3), 719 (2013).
7. X. P. Chen, C. K. Y. Wong, C. A. Yuan, and G. Q. Zhang, *Sensor Actuat B-Chem*, **177**, 178 (2013).
8. C. M. Lieber, *MRS Bull.*, **36**(12), 1052 (2011).
9. R. X. Yan, D. Gargas, and P. D. Yang, *Nat. Photon.*, **3**(10), 569 (2009).
10. Y. Cui, Q. Wei, H. Park, and C. M. Lieber, *Science*, **293**(5533), 1289 (2001).
11. T. Mårtensson, C. P. T. Svensson, B. A. Wacaser, M. W. Larsson, W. Seifert, K. Deppert, A. Gustafsson, L. R. Wallenberg, and L. Samuelson, *Nano Lett.*, **4**(10), 1987 (2004).
12. A. I. Boukai, Y. Bunimovich, J. Tahir-Kheli, J. K. Yu, W. A. Goddard, 3rd, and J. R. Heath, *Nature*, **451**(7175), 168 (2008).
13. C. O'Dwyer, M. Szachowicz, G. Visimberga, V. Lavayen, S. B. Newcomb, and C. M. S. Torres, *Nat. Nano.*, **4**(4), 239 (2009).
14. X. Liu, Y.-Z. Long, L. Liao, X. Duan, and Z. Fan, *ACS Nano*, **6**(3), 1888 (2012).
15. Y. Cui, Z. Zhong, D. Wang, W. U. Wang, and C. M. Lieber, *Nano Lett.*, **3**(2), 149 (2003).
16. N. S. Ramgir, Y. Yang, and M. Zacharias, *Small*, **6**(16), 1705 (2010).
17. S. Narayanan, J. R. Hajzus, C. E. Treacy, M. R. Bockstaller, and L. M. Porter, *ECS J. Solid State Sci. Technol.*, **3**(11), P363 (2014).
18. L. Mikyung and Y. Kijung, *Nanotechnology*, **23**(19), 194014 (2012).
19. B. Liu, C.-H. Wu, J. Miao, and P. Yang, *ACS Nano*, **8**(11), 11739 (2014).
20. M. H. Huang, S. Mao, H. Feick, H. Yan, Y. Wu, H. Kind, E. Weber, R. Russo, and P. Yang, *Science*, **292**(5523), 1897 (2001).
21. P. J. Pauzauskie, D. J. Sirbuly, and P. Yang, *Phys. Rev. Lett.*, **96**(14), 143903 (2006).
22. J. W. Lee, B. U. Ye, D.-y. Kim, J. K. Kim, J. Heo, H. Y. Jeong, M. H. Kim, W. J. Choi, and J. M. Baik, *ACS Appl. Mater. Interfaces*, **6**(3), 1375 (2014).
23. B. Park, I.-G. Bae, and Y. H. Huh, *Sci. Rep.*, **6**, 19485 (2016).
24. P. Mokarian-Tabari, R. Senthamaraikannan, C. Glynn, T. W. Collins, C. Cummins, D. Nugent, C. O'Dwyer, and M. A. Morris, *Nano Lett.*, **17**(5), 2973 (2017).
25. X. Yan, D. J. Poxson, J. Cho, R. E. Welser, A. K. Sood, J. K. Kim, and E. F. Schubert, *Adv. Func. Mater.*, **23**(5), 583 (2013).
26. S. P. Arnold, S. M. Prokes, F. K. Perkins, and M. E. Zaghloul, *Appl. Phys. Lett.*, **95**(10), 103102 (2009).
27. A. Klamchuen, M. Suzuki, K. Nagashima, H. Yoshida, M. Kanai, F. Zhuge, Y. He, G. Meng, S. Kai, S. Takeda, T. Kawai, and T. Yanagida, *Nano Lett.*, **15**(10), 6406 (2015).
28. W. McSweeney, O. Lotty, N. V. V. Mogili, C. Glynn, H. Geaney, D. Tanner, J. D. Holmes, and C. O'Dwyer, *J. Appl. Phys.*, **114**(3), 034309 (2013).
29. L. Dupré, D. Buttard, C. Leclere, H. Renevier, and P. Gentile, *Chem. Mater.*, **24**(23), 4511 (2012).
30. C. Glynn and C. O'Dwyer, *Adv. Mater. Interfaces*, **4**(2), 1600610 (2017).
31. D. R. Ceratti, B. Louis, X. Paquez, M. Faustini, and D. Grosso, *Adv. Mater.*, **27**(34), 4958 (2015).
32. A. T. Bellew, A. P. Bell, E. K. McCarthy, J. A. Fairfield, and J. J. Boland, *Nanoscale*, **6**(16), 9632 (2014).
33. O. Lotty, S. Biswas, T. Ghoshal, C. Glynn, C. O' Dwyer, N. Petkov, M. A. Morris, and J. D. Holmes, *J. Mater. Chem. C*, **1**(29), 4450 (2013).
34. C. Glynn, D. McNulty, H. Geaney, and C. O'Dwyer, *Small*, **12**(43), 5954 (2016).
35. C. Glynn, H. Geaney, D. McNulty, J. Connell, J. Holmes, and C. Dwyer, *J. Vac. Sci. Technol. A*, **35**(2), 020602 (2017).
36. C. Glynn, D. Aureau, G. Collins, S. O'Hanlon, A. Etcheberry, and C. O'Dwyer, *Nanoscale*, **7**(47), 20227 (2015).
37. J. Schindelin, C. T. Rueden, M. C. Hiner, and K. W. Eliceiri, *Mol. Reprod. Dev.*, **82**(7-8), 518 (2015).
38. C. A. Schneider, W. S. Rasband, and K. W. Eliceiri, *Nat. Meth.*, **9**(7), 671 (2012).
39. S. O'Hanlon, C. Glynn, and C. O'Dwyer, *ECS J. Solid State Sci. Technol.*, **5**(1), R3100 (2015).
40. C. Diaz, G. Barrera, M. Segovia, M. L. Valenzuela, M. Osiak, and C. O'Dwyer, *J Nanomater*, **2015**, 13 (2015).
41. C. Glynn, D. Creedon, H. Geaney, J. O'Connell, J. D. Holmes, and C. O'Dwyer, *ACS Appl. Mater. Interfaces*, **6**(3), 2031 (2014).
42. J.-Y. Lee, S. T. Connor, Y. Cui, and P. Peumans, *Nano Lett.*, **8**(2), 689 (2008).
43. D. Buckley, R. McCormack, and C. O'Dwyer, *J. Phys. D*, **50**(16), 16LT01 (2017).
44. H. K. Raut, V. A. Ganesh, A. S. Nair, and S. Ramakrishna, *Energy Environ. Sci.*, **4**(10), 3779 (2011).
45. X. Yu, T. J. Marks, and A. Facchetti, *Nat. Mater.*, **15**(4), 383 (2016).
46. L. Philippe and G. M. Morris, *Nanotechnology*, **8**(2), 53 (1997).
47. S. A. Boden and D. M. Bagnall, *Appl. Phys. Lett.*, **93**(13), 133108 (2008).
48. K. Choi, S. H. Park, Y. M. Song, Y. T. Lee, C. K. Hwangbo, H. Yang, and H. S. Lee, *Adv. Mater.*, **22**(33), 3713 (2010).
49. Y.-F. Huang, S. Chattopadhyay, Y.-J. Jen, C.-Y. Peng, T.-A. Liu, Y.-K. Hsu, C.-L. Pan, H.-C. Lo, C.-H. Hsu, Y.-H. Chang, C.-S. Lee, K.-H. Chen, and L.-C. Chen, *Nat. Nano*, **2**(12), 770 (2007).
50. L.-K. Yeh, K.-Y. Lai, G.-J. Lin, P.-H. Fu, H.-C. Chang, C.-A. Lin, and J.-H. He, *Adv. Energ. Mater.*, **1**(4), 506 (2011).
51. K. X. Wang, Z. Yu, V. Liu, Y. Cui, and S. Fan, *Nano Lett.*, **12**(3), 1616 (2012).
52. M. G. Deceglie, V. E. Ferry, A. P. Alivisatos, and H. A. Atwater, *Nano Lett.*, **12**(6), 2894 (2012).
53. B. Snaith, S. D. Probert, and P. W. O'Callaghan, *Appl. Energy*, **22**(1), 31 (1986).
54. M. M. Yovanovich, *IEEE Trans. Adv. Packag.*, **28**(2), 182 (2005).
55. R. L. Jackson, S. H. Bhavnani, and T. P. Ferguson, *J. Heat Transfer*, **130**(8), 081301 (2008).
56. J. W. Gooch, in *Encyclopedic Dictionary of Polymers*, J. W. Gooch, ed., p. 323, Springer New York, New York, NY, (2011).
57. G. Chen, *J. Nanopart. Res.*, **2**(2), 199 (2000).
58. D. G. Cahill, W. K. Ford, K. E. Goodson, G. D. Mahan, A. Majumdar, H. J. Maris, R. Merlin, and S. R. Phillpot, *J. Appl. Phys.*, **93**(2), 793 (2003).
59. S. Kucharski and G. Starzynski, *Wear*, **311**(1), 167 (2014).